

# Crack formation beneath sliding spherical punches

R. MOUGINOT

*Etablissement Technique Central de l'Armement, 16bis Avenue Prieur de la Cote D'Or, 94114 Arcueil Cedex, France*

Using Hamilton's equations (1983) for computing the stress trajectories corresponding to the crack path, and the method proposed by Mouginot and Maugis (1985), based on Lawn's analysis (1967) it is possible to express the strain energy release rate  $G$ , for various crack initiation radii and various friction coefficients. The initial radius of the crack can then be determined by maximizing  $G$ , and the critical load required to initiate it can be computed by application of the Griffith criterion, as a function of the following parameters: the elastic characteristics of the materials, the punch radius, the initial flaw size and the friction coefficient. The analysis proposed by Gilroy and Hirst is shown to be the lower bound of this theory. The theoretical results are compared with published experimental results, and are discussed.

## 1. Introduction

In 1967 Frank and Lawn [1] proposed a theoretical analysis for the Hertzian crack initiation, which was based on the energy balance (Griffith's criterion [2]) and the Hertz–Huber's stress field [3, 4]. They computed the strain energy release rate function  $\Phi$  which is a normalized expression of the strain energy release rate,  $G$  depending on the normalized crack size  $c/a$ . However, their assumptions were not in agreement with experiments (they supposed that starting radius of the crack was at the edge of the contact circle, and that the Poisson's ratio was  $\nu = 0.33$ ). Wilshaw [5] and later Warren [6] have shown that these assumptions were too restrictive and altered the estimation of the  $\Phi$  function.

Recently, Mouginot and Maugis [7] proposed a new analysis for crack initiation under cylindrical flat or spherical punches, using Lawn's method. Their computation of the  $\Phi$  function for various starting radii and for  $\nu = 0.22$  (the effect of the Poisson's ratio is also studied) leads to an explanation of the Auerbach's law [8] based on the low variation (with the relative flaw size  $c_f/a$ ) of  $\Phi$  on the envelope of the curves near its maximum. Crack initiation radii and critical loads are computed as function of the normalized flaw size  $c_f/a$ . The critical loads can also be determined as function of  $R/c_f^{3/2}$ , a parameter which does not depend on the increasing contact radius,  $R$  being the radius of the spherical punch. These computations were shown to be in agreement with experiments on optical glass.

The method described in [7] will now be extended to crack initiation under hertzian sliding contact. Lawn proposed in 1967 [9] a similar study, but based on still too restrictive assumptions, as pointed out by Enomoto [10]. Gilroy and Hirst [11] gave an analysis based on the assumption that the failure occurs at the same maximum tensile stress beneath a sliding contact as that beneath a normal hertzian one. This analysis will

be further discussed. Hamilton and Rawson [12] proposed a flaw statistic analysis of that problem and Lawn *et al.* (1984) [13] studied the equilibrium of the formed partial cone crack under a sliding hertzian contact. The failure process under elastic–plastic contact (sharp indenter) with tangential loading was studied by Swain [14]. The stress field for Hertzian sliding contact was determined in cartesian coordinates by Hamilton and Goodman [15] in 1966 and given explicitly by Hamilton [16] in 1983.

The analytical method will be described and compared with experimental results obtained by Gilroy and Hirst [11] (1969), by Enomoto [10], by Chiang and Evans [17], by Powell and Tabor [18] and by Barquins *et al.* [19]. Geometrical aspects of the problem are described in Fig. 1.

## 2. The stress field

The stress equations have been given by Hamilton [16] in an explicit form, with typographical mistakes corrected in Appendix A. The contours of the normalized principal stresses in the symmetry plane  $y = 0$  are

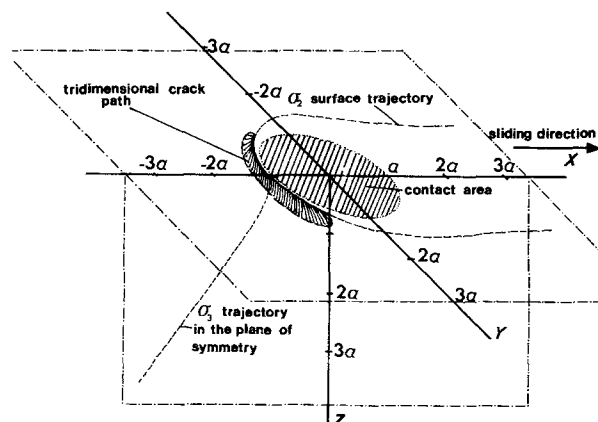


Figure 1 Tridimensional aspects of the problem; the crack path is drawn after [13, 19, 22].

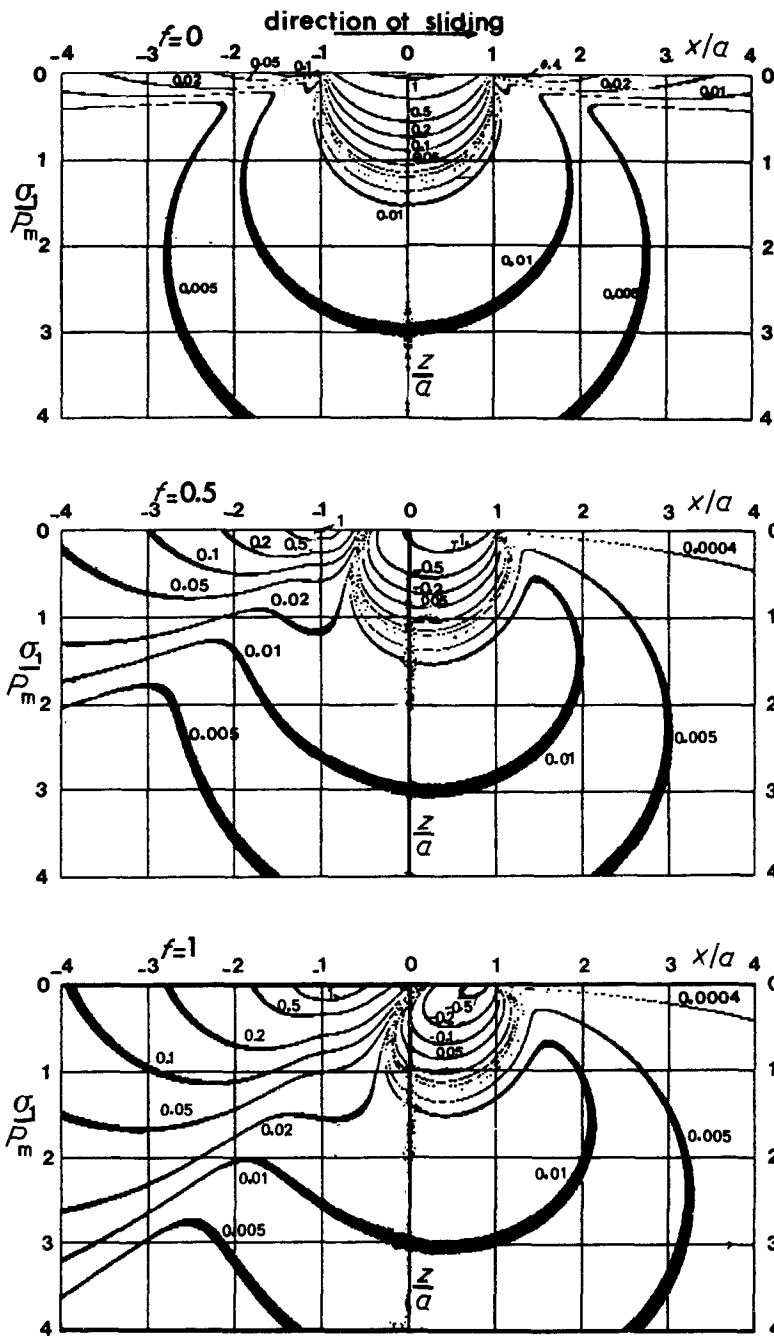


Figure 2 Contours of the normalized principal stress  $\sigma_1$  in the symmetry plane for  $f = 0, f = 0.5$  and  $f = 1.0$  and with a Poisson's ratio  $\nu = 0.25$ .

here completely numerically computed and are shown in Figs 2, 3 and 4 for the friction coefficients  $f = 0; f = 0.5$  and  $f = 1$ . The principal stress trajectories in the same plane are plotted in Fig. 5. The  $\sigma_2$  stress trajectory in surface starting from the point  $(-1, 0, 0)$  is shown in Fig. 6 for various friction coefficients. All these figures have been established with a Poisson's ratio  $\nu = 0.25$ . On the surface, according to Way [20] the stresses outside the contact area do not depend on the stress distribution inside the contact area. They are the same as those given by Swain [14] for a concentrated force (with typographical mistakes corrected in Appendix B), from Mindlin's computation [21]. This point was numerically verified [22]. The following equations, from Hamilton's paper [16], are given for the surface along the  $x$ -axis outside the contact circle (the contact radius  $a$  is taken as  $a = 1$ ), in normalized coordinates:

$$\frac{\sigma_1}{P_m} = \frac{1}{2} \left\{ \frac{1 - 2\nu}{x^2} + \frac{3}{4}f \left[ (4 + \nu) \left\{ \frac{(x^2 - 1)^{1/2}}{x} - x \operatorname{tg}^{-1} \left[ \frac{1}{(x^2 - 1)^{1/2}} \right] \right\} - 2\nu \frac{(x^2 - 1)^{1/2}}{x^3} \right] \right\} \quad (1)$$

$$\frac{\sigma_2}{P_m} = \frac{1}{2} \left( -\frac{1 - 2\nu}{x^2} + \frac{3}{4}f \left\{ \frac{(x^2 - 1)^{1/2}}{x^3} (1 + \frac{3}{2}x^2) - \frac{3}{2}x \operatorname{tg}^{-1} \left[ \frac{1}{(x^2 - 1)^{1/2}} \right] \right\} \right) \quad (2)$$

with

$$P_m = \frac{P}{\pi a^2}$$

### 3. The fracture analysis

The analysis is based on the following assumptions:

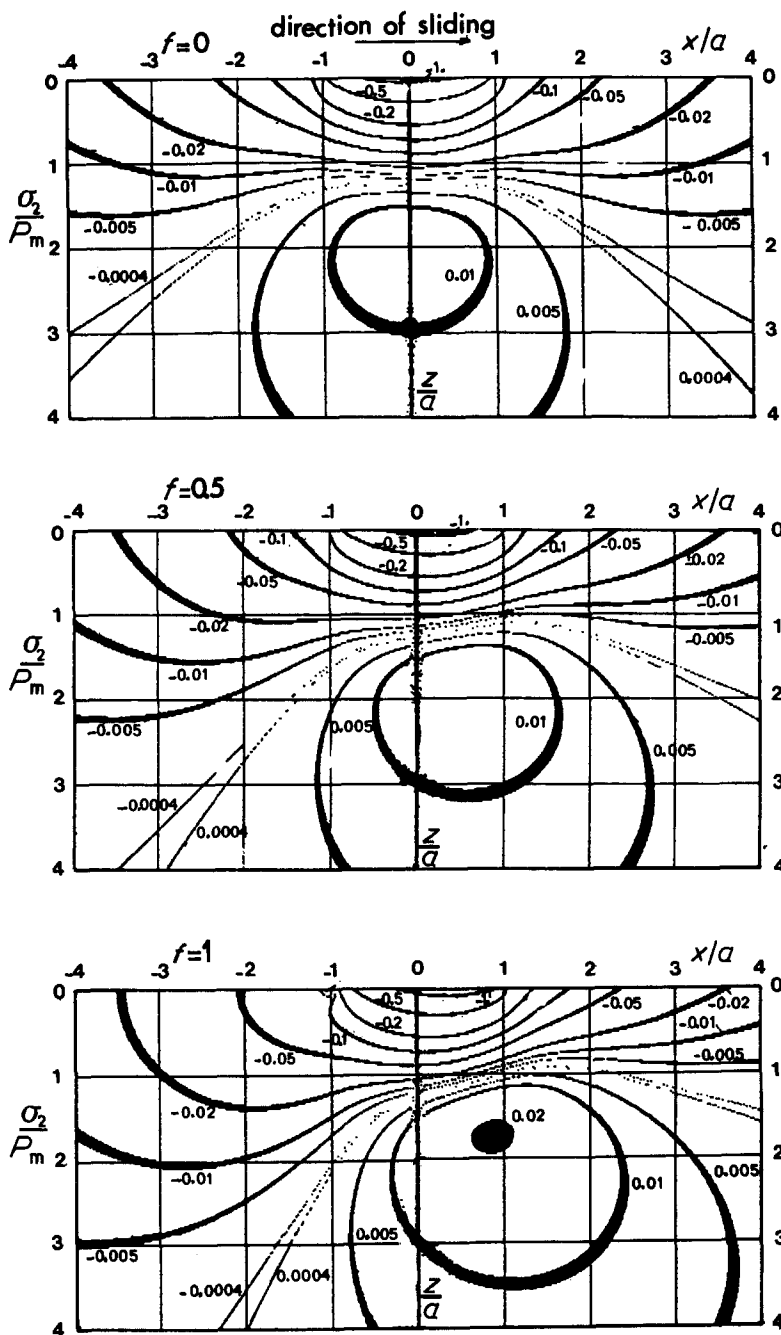


Figure 3 Contours of the normalized principal stress  $\sigma_2$  in the symmetry plane for  $f = 0, f = 0.5$  and  $f = 1.0$  and with a Poisson's ratio  $\nu = 0.25$ .

(i) The crack initiates on the surface “behind” the contact circle, on the  $x$ -axis. The starting locus  $x_0/a$  of the crack on this axis will be written  $r_0/a$  and named starting radius of the crack, by comparison with the hertzian fracture under normal loading.

(ii) The crack path follows the surface defined by  $\sigma_2 - \sigma_3$  stress trajectories (starting from points  $(x, 0, 0)$ ), i.e. it follows the corresponding  $\sigma_3$  stress trajectory in the plane  $y = 0, x < -a$ ,  $a$  being the contact radius. Experimental observations show that the tri-dimensional crack shapes always look like the computed shapes of the corresponding surfaces described by the stress trajectories [10, 19, 22].

(iii) The stress intensity factor, generally given for hertzian crack by:

$$K_I = 2 \left( \frac{c}{\pi} \right)^{1/2} \int_0^c \frac{r_b}{r_c} \frac{\sigma_1(b)}{(c^2 - b^2)^{1/2}} db \quad (3)$$

which has been derived for an internal crack of length

$2c$  in an infinite plate, subjected to a normal tensile stress  $\sigma_1(b)$  along its length.

The correction term  $r_b/r_c$  has been introduced because of the conical geometry of the studied crack [4]. In the case of sliding contact with friction coefficient larger than 0.39 conical crack path are not close any more, for  $\nu = 0.25$ . Although the crack geometry is no longer axisymmetrical, the  $r_b/r_c$  correction factor has been maintained. This is justified by its lower effect at high friction coefficient values.

(iv) For using this  $K_I$  estimation scheme it is necessary to assume that the normal tensile stress repartition  $\sigma_1(b)$  on the crack path in the symmetry plane  $y = 0$  does not vary too much on the both sides of this plane. Fig. 7 shows that the  $\sigma_1$  gradient along a  $\sigma_2$  trajectory is lower than that along the corresponding  $\sigma_3$  trajectory (the  $\sigma_1$  stress repartition is computed in Fig. 7 along  $\sigma_2$  and  $\sigma_3$  stress trajectories starting from point  $(-1, 0, 0)$ ). The larger the friction coefficient the

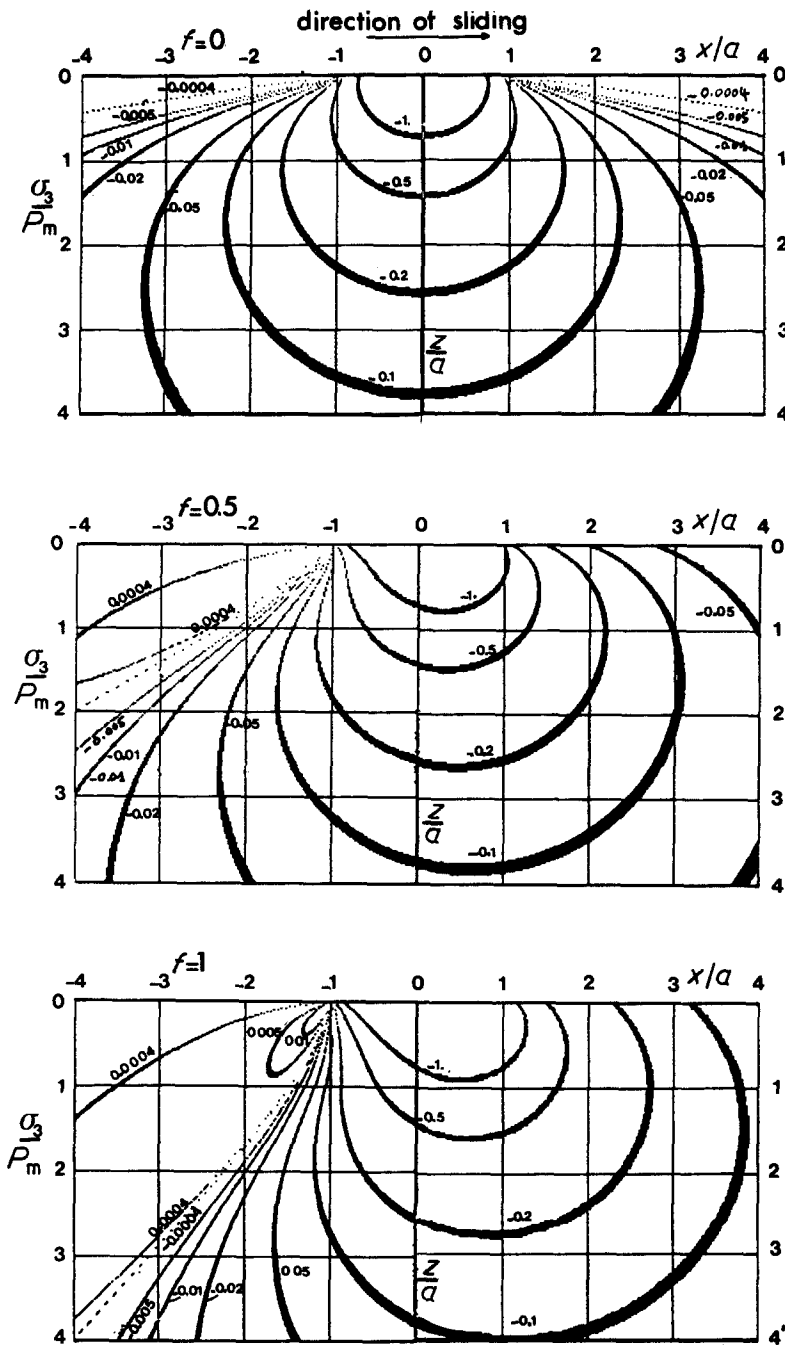


Figure 4 Contours of the normalized principal stress  $\sigma_3$  in the symmetry plane for  $f = 0$ ,  $f = 0.5$  and  $f = 1.0$  and with a Poisson's ratio  $\nu = 0.25$ .

larger the maximum of  $\sigma_1$  and the steeper the  $\sigma_1$  stress gradient along the  $\sigma_2$  and  $\sigma_3$  stress trajectories. It will be assumed, as for any tridimensional crack that the crack front is in a locally plane strain situation near the symmetry plane and that the stress distribution along the  $\sigma_3$  trajectory varies only slightly on both sides of the symmetry plane when  $(c_f/a) < 0.1$ . Then:

$$G = \frac{1 - \nu^2}{E} K_1^2 \quad (4)$$

where  $\nu$  and  $E$  are respectively the Poisson's ratio and the Young modulus of the indented material. By inserting Equation 3 into Equation 4 we obtain:

$$G = \frac{4}{\pi^3} \frac{1 - \nu^2}{E} \frac{P^2}{a^3} [\Phi(c/a)]_{r_0/a, f, \nu} \quad (5)$$

with

$$[\Phi(c/a)]_{r_0/a, f, \nu} = \frac{c}{a} \left[ \int_0^{c/a} \frac{r_b}{r_c} \frac{f(b/a)}{\left(\frac{c^2}{a^2} - \frac{b^2}{a^2}\right)^{1/2}} db/a \right]^2 \quad (6)$$

where

$$f(b/a) = \frac{\sigma_1(b/a)}{P_m}$$

with

$$P_m = \frac{P}{\pi a^2} \quad (7)$$

The strain energy release rate function  $\Phi$  is plotted in Fig. 8 for  $f = 0$ ,  $f = 0.2$ ,  $f = 0.5$  and  $f = 1.0$ , respectively. As  $f$  increases both the maximum of the  $\Phi$  curve envelope and the corresponding crack size become larger.

If the initial flaw size  $c_f/a$  is very small, say  $c_f/a < 0.001$ ,  $\sigma_1$  may be considered as constant along it and given by Equation 1 (undiminishing stress field). The analytical integration of Equation 6 gives then:

$$G = \frac{1 - \nu^2}{\pi} \left[ \frac{1 - 2\nu}{2} \left( 1 + \frac{3}{8} f \pi \frac{4 + \nu}{1 - 2\nu} \right) \right]^2 \times \frac{P^2}{E a^3} \left( \frac{a}{r_0} \right)^4 \frac{c_f}{a} \quad (8)$$

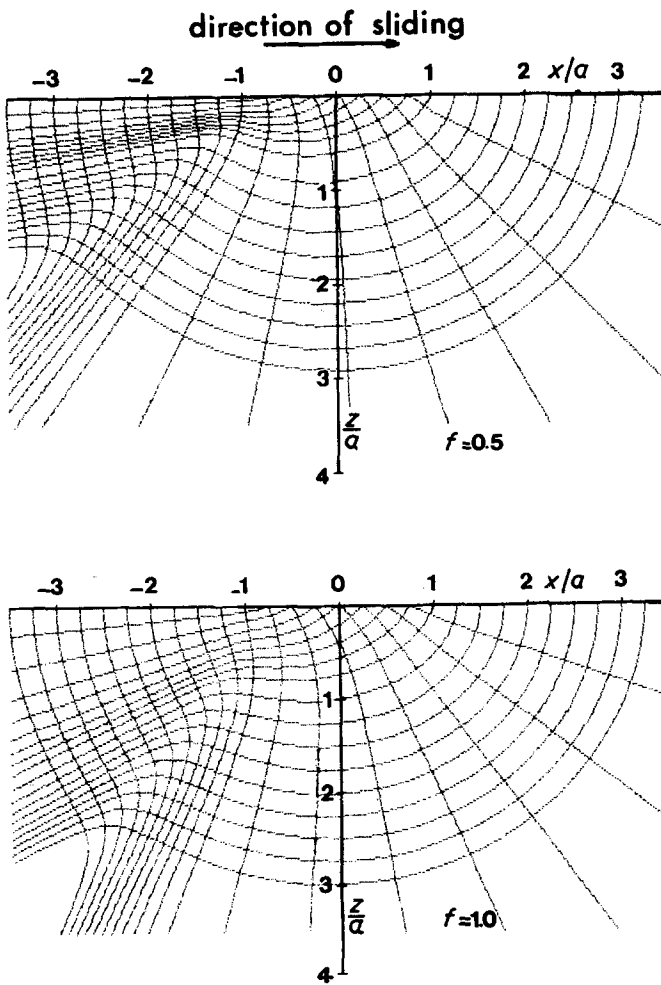


Figure 5 Stress trajectories in the plane of symmetry for the friction coefficients  $f = 0.5$  and  $f = 1.0$  with  $\nu = 0.25$ .

#### 4. Initiation of the partial cone crack

##### 4.1. Starting radius of the crack

Under hertzian contact, it has been observed experimentally that cracks will initiate outside the contact edge. A simple explanation was given in a previous paper [7]: for a given initial flaw size  $c_f/a$ , a crack will start at the radius where the strain energy release rate is maximum,  $a$  being the contact radius just before failure. Moreover, Johnson *et al.* [23] have shown that the hertzian stress field is modified by the elastic mismatch between the indenter and the specimen and that, due to interfacial shear stresses, the maximum tensile stress acts in surface outside the circle of contact. However, the computation with Hamilton's equations gives a maximum tensile stress at the edge of the contact circle.

The crack extension will then be governed by the  $\Phi(r_0/a)$  curve which is tangent to the envelope of the

$\Phi$  curves at the  $c_f/a$  abscissa. The starting radii  $r_0/a$  maximizing  $\Phi$  are plotted as a function of  $c_f/a$  on Fig. 9 for various friction coefficients. The starting radius decreases as  $f$  increases and for  $f > 0.4$ , the crack will always start at the edge of the contact, as shown in Fig. 10 where  $r_0/a$  is drawn as a function of  $f$  for some values of  $c_f/a$ .

##### 4.2. The critical load

Equation 5 and Griffith's criterion  $G = 2\gamma$  where  $\gamma$  is the surface energy lead to:

$$P_c = \left( \frac{\pi^3 E}{2(1 - \nu^2)} \gamma \right)^{1/2} \left\{ \frac{a^3}{[\Phi(c_f/a)]_{r_0/a,f}} \right\}^{1/2} \quad (9)$$

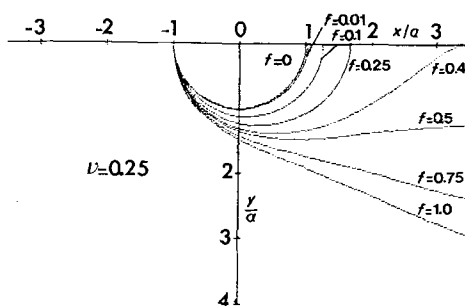


Figure 6 Stress trajectories of  $\sigma_2$  on the surface for various friction coefficients, starting from the point  $(-1, 0, 0)$ .

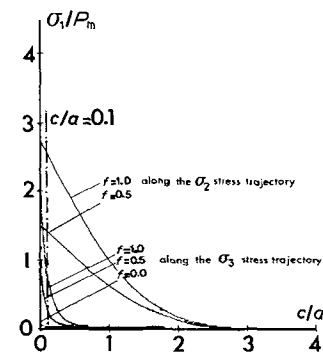


Figure 7  $\sigma_1$  stress repartition along the  $\sigma_2$  stress trajectory on surface and the  $\sigma_3$  stress trajectory in the symmetry plane, both starting from the point  $(-1, 0, 0)$ ,  $c/a$  is the normalized curvilinear coordinate along these trajectories. The curves are plotted for  $f = 0$ ,  $f = 0.5$  and  $f = 1$  with  $\nu = 0.25$ .

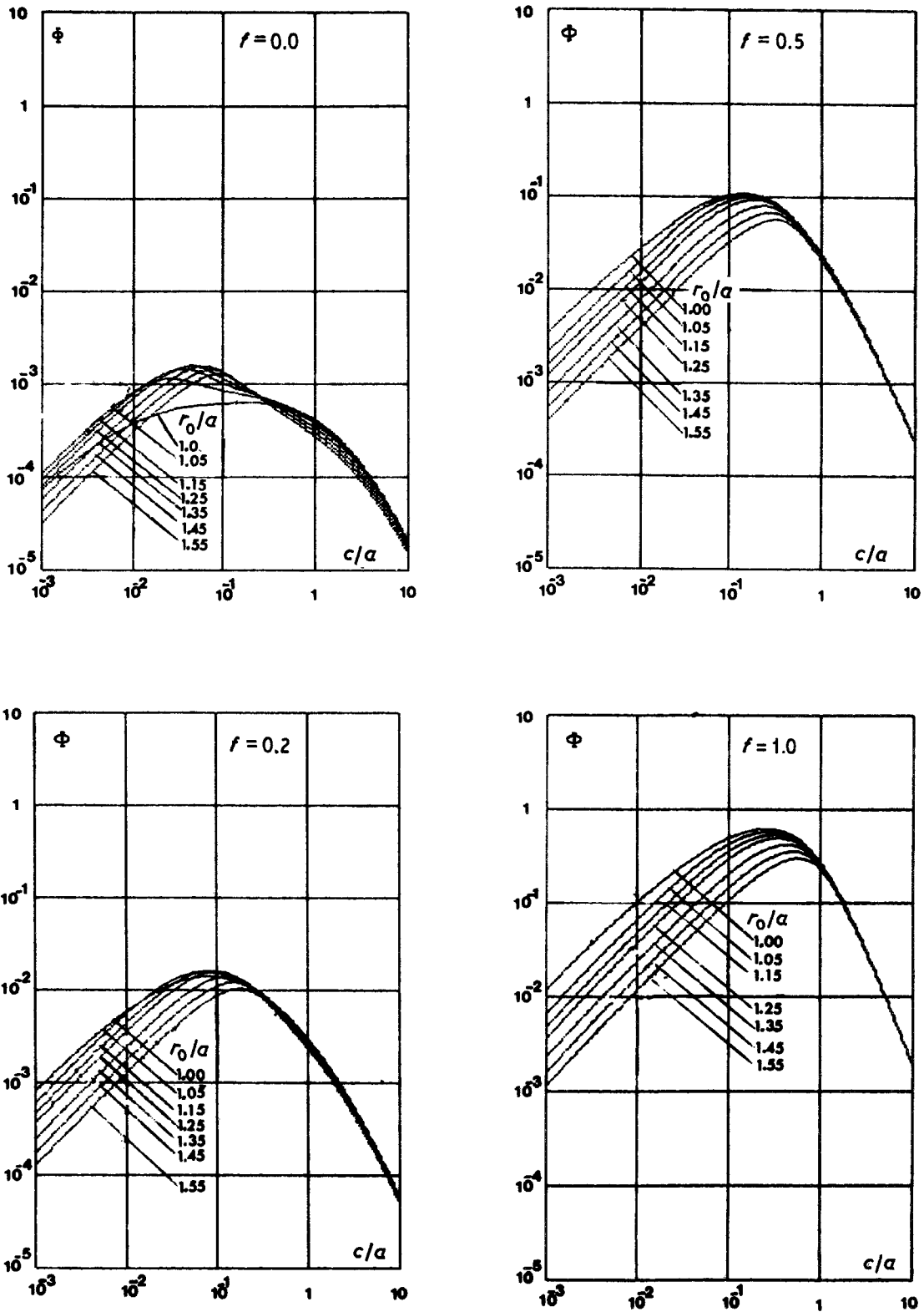


Figure 8 Strain energy release rate function  $\Phi$  against normalized crack length for various starting radii  $r_0/a$  and for  $f = 0, f = 0.2, f = 0.5$  and  $f = 1.0$ .

$[\Phi(c_f/a)]_{r_0/a, f}^{-1/2}$  is the normalized critical load for crack initiation and is plotted in Fig. 11 as a function of  $c_f/a$  for  $f = 0, f = 0.1, f = 0.25, f = 0.5$  and  $f = 1$ . Note that the critical load decreases as  $f$  increases and that Auerbach's range corresponding to the plateau of the curves shifts to higher  $c_f/a$  values according to the general  $\Phi$  curves of Fig. 8. In Fig. 12 the ratio  $P_{cf}/P_{CN}$  between the critical load under sliding contact with a given  $f$  and critical load under normal Hertzian contact is drawn at a given normalized flaw size  $c_f/a$ . ( $a$  is the contact radius just before crack initiation).

When the initial flaw size  $c_f/a$  is very small, (undiminishing stress field) and  $\Phi$  function is then easily determined. We find, using Equation 8:

$$P_c = \left\{ \frac{8\pi E\gamma}{(1-v^2)[1-2v+\frac{3}{8}f\pi(4+v)]^2} \right\}^{1/2} \times \left(\frac{a}{c_f}\right)^{1/2} \left(\frac{r_0}{a}\right)^2 a^{3/2} \quad (10)$$

But, as shown in the previous paper [7], Equation 9 is not very convenient because of the variation of the

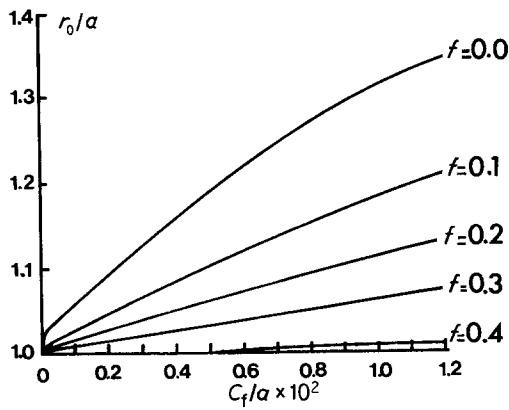


Figure 9 Normalized starting radius of the crack as function of the reduced flaw size for some values of the friction coefficient.

contact radius with the applied load, so that the initial flaw size depends on the load. Following the method described in [7], it is possible, by using Hertz's relation:

$$a^3 = \frac{3}{4} \left( \frac{1 - \nu^2}{E} \right) kPR \quad (11)$$

in Equation 9, to express  $P_c$  as:

$$P_c = \frac{3\pi^3}{8[\Phi(c_f/a)]_{r_0/a, f, \nu}} k\gamma R \quad (12)$$

where

$$k = 1 + \frac{1 - \nu^2}{1 - \nu^2} \frac{E}{E'} \quad (13)$$

( $k = 1$  for rigid indenters and  $k = 2$  for identical materials).  $\Phi(c_f/a)$  is determined on the envelope of the  $\Phi$  curves by the intersection with the straight lines given (not plotted, see [7]) by:

$$[\Phi(c_f/a)]_{r_0/a, f, \nu} = \frac{g\pi^3(1 - \nu^2)}{32} \gamma \frac{R^2 k^2}{Ec_f^3} \left( \frac{c_f}{a} \right)^3 \quad (14)$$

obtained by eliminating  $P_c$  between Equations 11 and 12. One can then plot  $P_c/\gamma R$  as function of  $R/c_f^{3/2}$  in Fig. 13, which does not depend on the contact radius. For each friction coefficient, there is a range of  $R/c_f^{3/2}$  where  $P_c/\gamma R$  has a plateau as expected from Figs 8 and 11; in this range, the  $P_c$ - $R$  relation follows Auerbach's law.

For plotting the Fig. 13  $\gamma/E = 5 \cdot 10^{-11}$  m was taken, which is a representative value for glass.

In Auerbach's range,  $\Phi$  remains constant and  $\gamma$  can

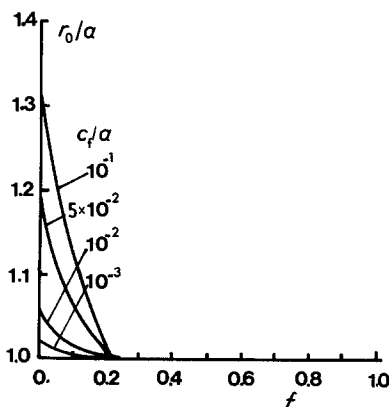


Figure 10 Normalized starting radius of the crack as function of the friction coefficient for some values of the reduced flaw size.

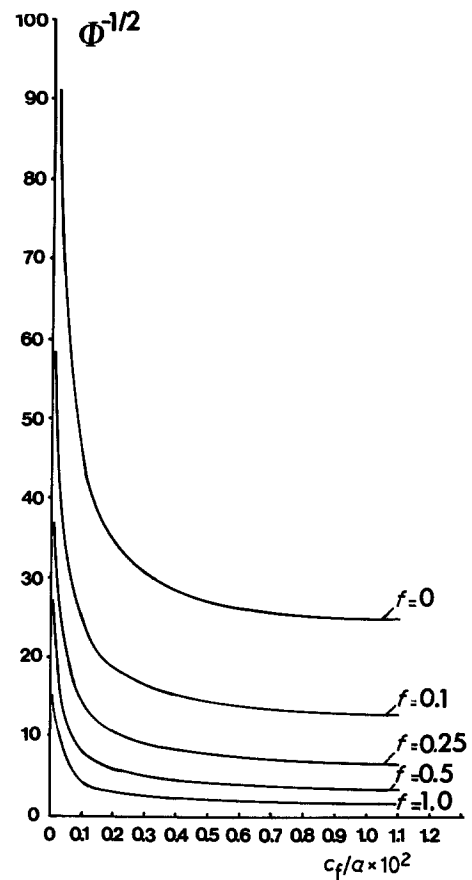


Figure 11 Normalized critical load  $[\Phi(c_f/a)]_{r_0/a, f}^{-1/2}$  as function of the reduced flaw size for various friction coefficients.

be easily determined by:

$$\gamma = A(f)P_c/kR \quad (15)$$

where  $A(f)$  depends on  $f$  and on the Poisson's ratio, and is given by the maximum of the envelope of  $\Phi$ . For example (with  $\nu = 0.22$ ):

$$\begin{aligned} \text{for } f = 0 & \quad \gamma = 1.49 \cdot 10^{-4} P_c/kR \\ \text{for } f = 0.2 & \quad \gamma = 1.43 \cdot 10^{-3} P_c/kR \\ \text{for } f = 0.5 & \quad \gamma = 1 \cdot 10^{-2} P_c/kR \end{aligned}$$

(16)

On Fig. 13 straight lines corresponding to constant  $c_f/a = 0.1$  for  $k = 1$  and  $k = 2$ , which are limits for a validity of this analysis are also plotted.

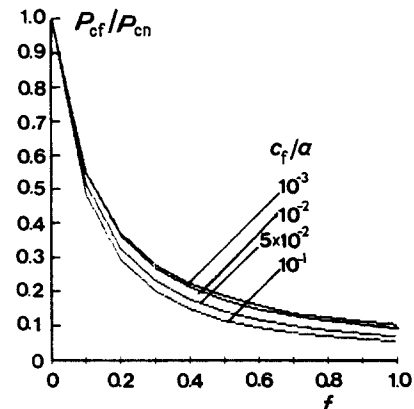


Figure 12 Ratio of critical loads beneath sliding against normal hertzian contact at some constant values of the reduced flaw size, as a function of the friction coefficient.

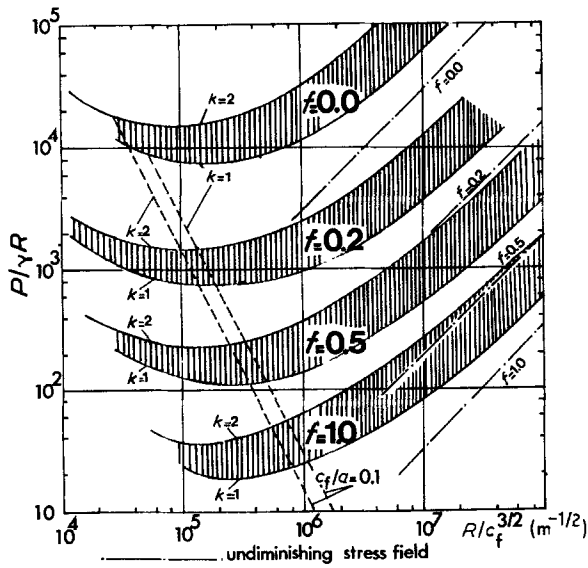
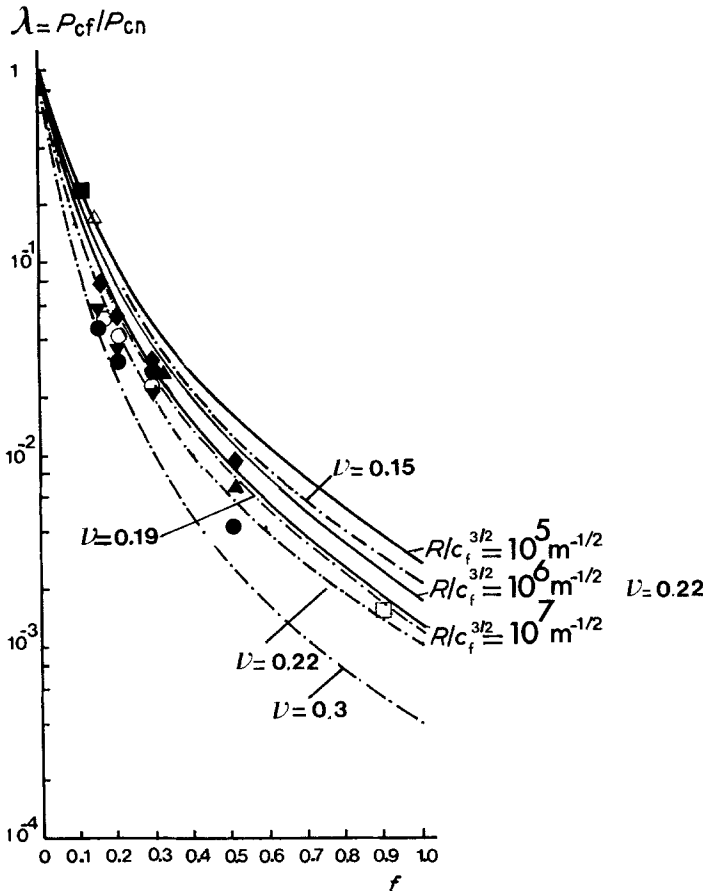


Figure 13 Critical load as function of the radius of the punch in normalized coordinates, given for  $k = 1$  (rigid punch) and  $k = 2$  (same materials) and for some coefficients of friction. Undiminishing stress field case is plotted for  $k = 1$ , and the limit of the flaw size is plotted for  $k = 1$  and  $k = 2$ .

The  $\lambda = P_{cf}/P_{cN}$  ratio between a critical load  $P_{cf}$  at a given  $f$  and the critical load  $P_{cN}$  for the normal hertzian contact is given from Equation 12 by:

$$\lambda = \frac{[\Phi(c_f/a)]_{r_0/a, f=0} \gamma^*}{[\Phi(c_f/a)]_{r_0/a, f} \gamma} \quad \text{for a given } R/c_f^{3/2} \quad (17)$$

where  $\gamma$  is the surface energy of the material indented by the hertzian method and  $\gamma^*$  is the modified surface energy during the sliding test. It is plotted for given



$R/c_f^{3/2}$  as a function of  $f$  in Fig. 14. The reduction factor  $\lambda$  for the critical load decreases strongly when the friction coefficient increases and it decreases slightly when the punch radius increases.

The critical load for an undiminishing stress field (very small  $c_f/a$ ) is given by:

$$P_c = \frac{9}{[1 - 2\nu + \frac{3}{8}f\pi(4 + \nu)]^3} \left\{ \frac{2\pi^3(1 - \nu^2)}{E} \right\}^{1/2} \times \frac{\gamma^{3/2} R^2 k^2}{c_f^{3/2}} \left( \frac{r_0}{a} \right)^6 \quad \text{for a given } R/c_f^{3/2} \quad (18)$$

by using Equation 10. It is also shown on Fig. 13 for the four values of  $f$ .

The ratio  $\lambda$  for undiminishing stress field is given by:

$$\lambda = \frac{1}{\left( 1 + \frac{3}{8}f\pi \frac{4 + \nu}{1 - 2\nu} \right)^3} \left( \frac{\gamma^*}{\gamma} \right)^{3/2} \quad (19)$$

For experiments performed in the same environments and with the same punch this equation becomes:

$$\lambda = \frac{1}{\left[ 1 + \frac{3}{8}f\pi \left( \frac{4 + \nu}{1 - 2\nu} \right) \right]^3} \quad (20)$$

This equation, first proposed by Gilroy and Hirst [11], corresponds to a lower bound for the reduction ratio  $\lambda$  given by the Equation 17. That limiting reduction factor is shown on Fig. 14 for  $\nu = 0.15$ ,  $\nu = 0.19$ ,  $\nu = 0.22$  and  $\nu = 0.3$ .

Gilroy and Hirst's reduction factor is based on the assumption that the failure occurs at the same maximum tensile stress beneath a sliding spherical contact and beneath a normal hertzian's one. This assumption

Figure 14  $\lambda$  ratio of critical loads for sliding against hertzian contact as function of the friction coefficient  $f$ , plotted for three values of the normalized punch radius and with  $\nu = 0.22$ . Dashed lines correspond to the same ratios in the undiminishing stress field case, given for  $\nu = 0.15, 0.19, 0.22$  and  $0.3$ . Experimental results from Gilroy and Hirst [11] and from Powell and Tabor [18] are also plotted. Gilroy and Hirst;  $\nabla$   $R = 2$  mm,  $\circ$   $R = 2.4$  mm,  $\bullet$   $R = 4.4$  mm,  $\blacktriangle$   $R = 4.8$  mm,  $\blacklozenge$   $R = 9.5$  mm. Powell and Tabor;  $\blacksquare$   $R = 0.55$  mm,  $\triangle$   $R = 5$  mm,  $\square$   $R = 6$  mm.

only holds in the case of an undiminishing stress field.

For larger initial flaws, subjected to a  $\sigma_1(b)$  normal tensile stress repartition this assumption would have no physical basis. Initial flaw will reach an equilibrium when  $G = 2\gamma$ , also under sliding contact and then the failure will occur when  $G_{\text{sliding}} = G_{\text{hertzian}} = 2\gamma$ .

It would be interesting to compare the maximum tensile stress for the sliding and the normal hertzian contact, at the edge of the contact, i.e. on the point  $(-1, 0, 0)$  for a given  $R/c_f^{3/2}$  value. This ratio has been obtained from Equation 1 and Equation 12 and the relation is:

$$\frac{\sigma_{m \text{ sliding}}}{\sigma_{m \text{ hertzian}}} = \left( 1 + \frac{3}{8} f \pi \frac{4 + \nu}{1 - 2\nu} \right) \left\{ \frac{[\Phi(c_f/a)]_{r_0/a, f=0}}{[\Phi(c_f/a)]_{r_0/a, f}} \right\}^{1/3} \quad (21)$$

This ratio is plotted in Fig. 15 as a function of the friction coefficient  $f$  for three values of  $R/c_f^{3/2}$ . It is equal to 1, as expected, in the case of the undiminishing stress field hypothesis. These curves confirm that the material does not fail at the same maximum tensile stress under sliding contact and under normal hertzian contact.

### 4.3. Auerbach's range

The dependence of Auerbach's range of the friction coefficient  $f$  can be estimated from Fig. 13. Because Auerbach's law corresponds to the maximum of the envelope of the  $\Phi$  curves, computing the abscissa  $R/c_f^{3/2}$  of this maximum at different  $f$  confirms this low variation: for  $f = 0$ ,  $R_m/c_f^{3/2} = 1.7 \times 10^5 \text{ m}^{-1/2}$  and for  $f = 1$ ,  $R_m/c_f^{3/2} = 2.8 \times 10^5 \text{ m}^{-1/2}$ .

Lawn [9] proposed that Auerbach's law does not apply when  $f > 0.02$ . This theory was based on the particular shape (two maxima) of the  $\Phi$  curve at  $r_0/a = 1$  and  $\nu = 0.33$ . With these values the  $\Phi$  curve has only one maximum if  $f > 0.02$ . This theory cannot explain the Auerbach's law when  $r_0/a > 1$  or  $\nu < 0.33$  for which experimental Auerbach's range has been measured, even under a normal Hertzian contact or under a sliding one. This was first pointed out by Wilshaw [5], Warren [6] and Enomoto [10].

### 4.4 Influence of the Poisson's ratio on $\lambda$

The huge influence of the Poisson's ratio on the strain

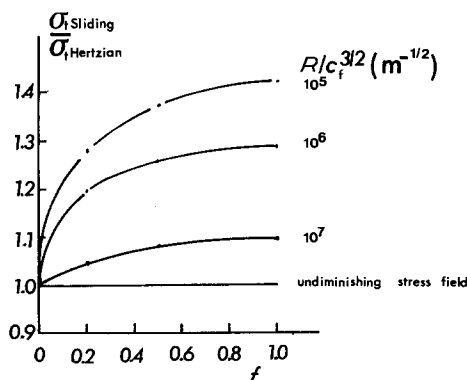


Figure 15 Ratios of the maximum tensile stresses beneath a sliding against a normal hertzian contact, computed at the critical loads and plotted for three values of the normalized radius of the punch and in the undiminishing stress field case.

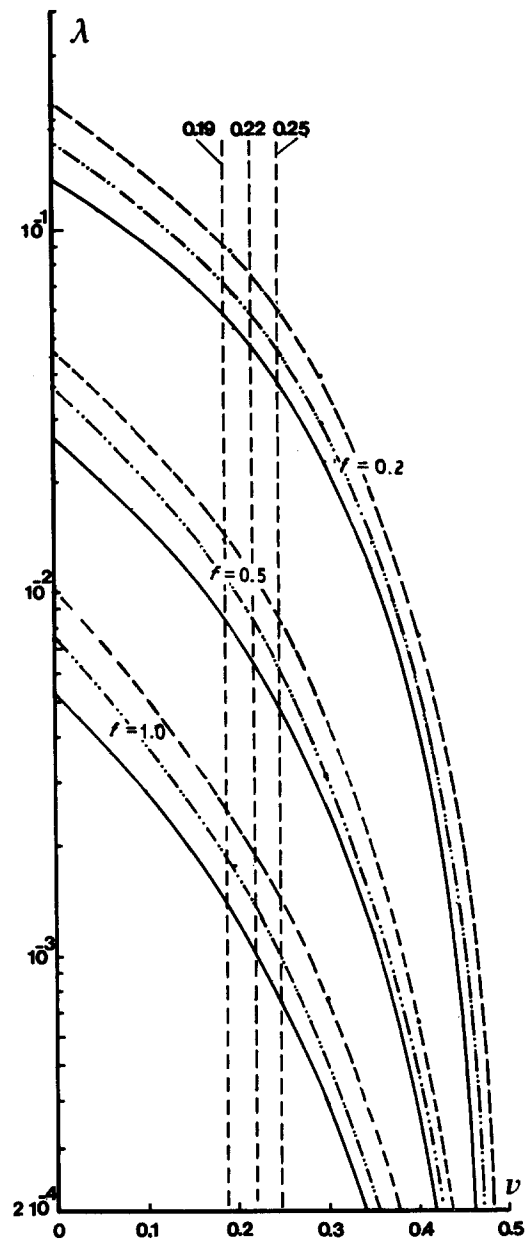


Figure 16  $\lambda$  as function of the Poisson's ratio for three values of the friction coefficient. For each value of  $f$  are plotted the curves corresponding to the undiminishing stress field case and to two values of the normalized punch radius. (---)  $R/c_f^{3/2} = 10^6 \text{ m}^{-1/2}$ , (-·-·-)  $R/c_f^{3/2} = 10^7 \text{ m}^{-1/2}$ , (—) undiminishing stress field.

energy release rate function was shown in the previous paper [7].

Its effect on the reduction ratio  $\lambda$  is now studied, first by computing  $\lambda$  in the undiminishing stress field case (Equation 20) then by computing this ratio in the general case given by Equation 17 for two values of  $R/c_f^{3/2}$ . These results are plotted in Fig. 16.

The ratio between the values of  $\lambda$  computed for an undiminishing stress field case to that computed for a given  $R/c_f^{3/2}$  remains approximately constant for the Poisson's ratio ranging between 0.19 and 0.25. It is then possible to correlate the results obtained with  $\nu = 0.19$  (TiC) to those obtained with  $\nu = 0.22$  (glass) as mostly assumed in this paper.

## 5. Experimental results and discussion

The experimental results obtained by Gilroy and Hirst [11], Enomoto [10], Powell and Tabor [18], and Barquins *et al.* [19] are reanalysed. Gilroy and Hirst

[11] like Enomoto run experiments on soda lime glass in various environmental liquids, Powell and Tabor on TiC and Barquins *et al.* on silicon. Experimental details are described in the concerned papers.

### 5.1. Starting radius of the crack

Gilroy and Hirst [11] and even Enomoto [10] gave no information about the starting radius of the crack. Lawn [9] noticed that “at  $f = 0.1$  the crack initiates from very near to the trailing edge of the indenter”. Powell and Tabor [18] gave more details on this point, they found normalized starting radii  $1.2 < r_0/a < 1.35$  for steel indenters on TiC plates. These values are much larger than the expected ones. Measurements with TiC indenters give  $r_0/a < 1$ , what is less than the expected value.

In fact, as for the hertzian fracture, the dispersion of the  $r_0/a$  measurements is large when the flaw size  $c_f/a$  is small. On the other hand, Fig 2 shows that the  $\sigma_1$  stress remains tensile in the contact circle when  $f > 0$  (contrary to the purely hertzian case), so that the crack can start in that zone beneath a sliding contact.

However, these values have been obtained with computed contact areas. As shown in the previous paper [7], the true contact radius is much larger than the computed one, due to the surface roughness. That could partially explain the discrepancies between the theory and the experimental measurements.

### 5.2. The critical load and the reduction ratio

Measured  $P_c/R$  on glass [10, 11] are shown in Fig. 17. The plotted lines are the theoretical predictions, computed from Equation 12 with  $\gamma = 3.2 \text{ J m}^{-2}$  for three

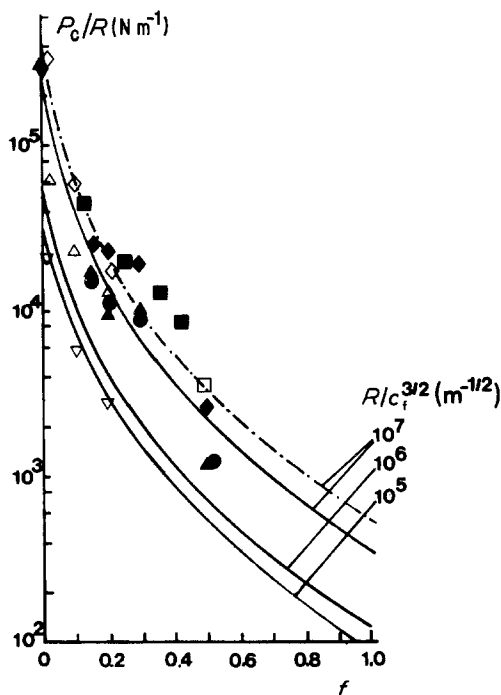


Figure 17 Normalized critical load as function of the friction coefficient. The theoretical predictions are plotted with two values of the fracture surface energy ( $\cdots$ )  $\gamma = 5 \text{ J m}^{-2}$ , ( $\text{—}$ )  $\gamma = 3.2 \text{ J m}^{-2}$ , and for three values of the normalized punch radius and they are compared with the experimental results of Enomoto [10];  $\square$   $R = 1 \text{ mm}$ ,  $\blacksquare$   $R = 2.5 \text{ mm}$ , and Gilroy and Hirst [11];  $\blacktriangledown$   $R = 2 \text{ mm}$ ,  $\bullet$   $R = 4.4 \text{ mm}$ ,  $\blacktriangle$   $R = 4.8 \text{ mm}$ ,  $\blacklozenge$   $R = 9.5 \text{ mm}$ , and Chiang and Evans [17];  $R = 1.6 \text{ mm}$   $\diamond$   $\text{Si}_3\text{N}_4$ ,  $\triangle$  glass (pristine),  $\nabla$  glass (abraded),  $k = 1.35$ .

values of  $R/c_f^{3/2}$  (continuous lines) and  $\gamma = 5.0 \text{ J m}^{-2}$  (dashed lines).

Experiments agree qualitatively well with the theoretical results.  $P_c/R$  decreases with  $R/c_f^{3/2}$  as predicted and the variation of  $P_c/R$  against  $f$  for a given punch radius confirms the theoretical results.

However a great dispersion is observed, probably due to the following causes:

1. The critical loads are measured in various environmental media (water, paraffin, air, etc.) which, as described by Enomoto [10], modify the intrinsic surface energy of the material. However, the initial flaws being always very small (except for the abraded glass specimen of Chiang and Evans [17]), the crack velocity is high (as proposed by Mougnot and Maugis [7]) and can even reach a critical speed corresponding to catastrophic failure. In this case adsorption effects are less important at crack tip and surface energy is less modified (Maugis [24]).

2. The friction coefficient is considered by these authors [10, 17] as being independent of the applied load. Results obtained by Powell and Tabor [18] on TiC show that for a given environmental medium the friction coefficient varies with the mean pressure proportional to  $(P/R^2)^{1/3}$  as plotted in Fig. 18. The increase of  $P_c/R$  with  $R$  at given  $f$  found by Gilroy and Hirst [11] can then be explained by an overvaluation of the friction coefficient. Results from Adewoye and Page [25] show that the friction coefficient must be measured carefully and at any stage of the loading since it varies strongly with the applied load.

The reduction factor between the critical loads under sliding and normal Hertzian contact can also be analysed. Gilroy and Hirst (glass) and Powell and Tabor (TiC) results, which are in good agreement with the theory, are plotted on Fig. 14. The continuous lines correspond to this theory for three values of  $R/c_f^{3/2}$ , while dashed lines correspond to the lower bound of this theory (given first by Gilroy and Hirst), plotted for different values of the Poisson's ratio.

Lawn's formula [9] is not plotted. It was based on wrong assumptions: the  $P^*$  critical load (corresponding to the local minimum of the  $\Phi$  curve) proposed by Lawn does not exist for  $\nu < 0.33$  and for normalized crack starting radii greater than 1. This is probably the greatest drawback of his analysis. The choice of the

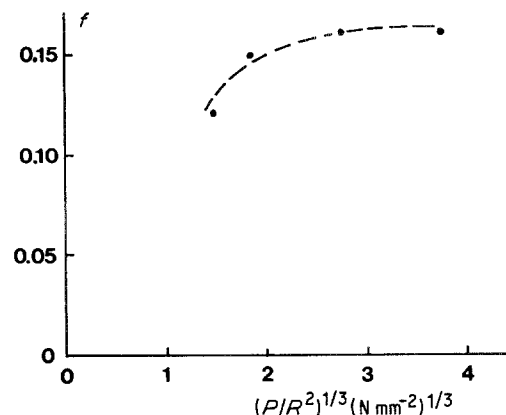


Figure 18 Friction coefficient as function of the normalized mean pressure. From results of Powell and Tabor [18].

TABLE I Comparison between critical load ratios obtained experimentally by Powell and Tabor [14] and the computed ones in the lower bound case (Gilroy and Hirst) and the general case

R (mm)	f	$\lambda$ (exp)	$\lambda$ (Gilroy and Hirst)	$\lambda$ (general method)	
				$c_f = 1 \mu\text{m}$	$c_f = 0.5 \mu\text{m}$
0.55	0.16	0.182	0.087	0.13	0.17
3	0.15	0.149	0.09	0.14	0.18
5	0.12	0.212	0.133	0.20	0.23

one-dimensional initial flaw geometry is probably less critical if the initial flaw size remains small in comparison with the contact radius.

When using Equation 20 Powell and Tabor [18] founded calculated values of  $\lambda$  lower than experimental ones. They are now compared (Table I) with the values obtained from Fig. 14 (Equation 17) and using the reasoning presented in Section 4.4 because experiments were made on TiC with a Poisson's ratio  $\nu = 0.19$  when the computation used  $\nu = 0.22$ .

These results may be compared with those of Chiang and Evans [17]. They made static contact experiments, leading to a partial slip situation. The friction coefficient is now given by the ratio  $T/N$  between the tangential and the normal components of the applied load on the inclined plate.  $f_0$  is the sliding friction coefficient and then  $T/N < f_0$ . We obtain from their results the values given in Table II.

These values of measured  $\lambda$  for the pristine glass are larger than those expected from the theory.

This discrepancy can be probably explained by the highly inhomogeneous flaw repartition of different sizes. Another explanation is given by the existence of shear stresses due to the elastic mismatch between indenter and specimen [23], which also causes the unloading crack initiation.

The values of  $\lambda$  measured for abraded glass and  $\text{Si}_3\text{N}_4$  are approximately in agreement with the theoretical prediction. Moreover the measured normalized critical loads  $P_c/R$  are in qualitatively good agreement with the theory as shown on Fig. 17.

### 5.3 Maximum tensile stress for failure

Results obtained by Barquins *et al.* [19] apparently seem to confirm the opinion of many authors that partial conical cracks initiate at the same maximum tensile stress than in the case of Hertzian fracture.

Barquins *et al.*, use Silicon specimens abraded with paper SiC 800. Then, an estimation of  $R/c_f^{3/2}$  leads to values close to  $10^5 \text{m}^{-1/2}$  (Langitan and Lawn [26]). The measurements have been made with friction coefficient between 0.23 and 0.5, a range in which the stress does not vary much as shown by Fig. 15. For  $0.23 < f < 0.5$  the ratio is close to 1.35 and is in agreement with the measured ratio 1.32 between the maximum tensile stress measured under sliding

contact by Barquins *et al.* [19] and that given by Lawn [27] for a normal Hertzian crack.

### 5.4. Fracture surface energy measurements

Fracture surface energy has been computed for the soda lime glass from Gilroy and Hirst's results [11] and Enomoto's one [10]. Using Equation 14, results of the first authors give surface energy values between  $1.05$  and  $3.2 \text{J m}^{-2}$  for  $R = 4.8 \text{mm}$  and between  $1.2$  and  $3.6 \text{J m}^{-2}$  for  $R = 9.5 \text{mm}$ . Surprisingly, sliding tests in water give higher values of  $\gamma$  than those run in air. With the measurements of Enomoto [10], one obtains more satisfactory results:  $\gamma = 3.2 \text{J m}^{-2}$  in air ( $f = 0.4$  and  $R = 2.5 \text{mm}$ ) and  $\gamma = 2.27 \text{J m}^{-2}$  in distilled water ( $f = 0.48$  and  $R = 2.5 \text{mm}$ ) which are in agreement with values calculated from normal Hertzian tests.

### 5.5. Auerbach's law

Fig. 12 shows that Auerbach's law applies for a given range of  $R/c_f^{3/2}$  even for  $f > 0$ . Gilroy and Hirst [11] found an Auerbach's range for glass with  $f$  values between 0.15 and 0.5 and Powell and Tabor [18] for TiC, with  $f = 0.15$  approximately.

Powell and Tabor [18] abraded their specimens with  $14 \mu\text{m}$  diamond paste assumed  $0.5 \mu\text{m} < c_f < 1 \mu\text{m}$  as  $c_f$  range and used indenter radii between 0.55 and 5 mm, so that  $R/c_f^{3/2}$  range is between  $55 \times 10^5 \text{m}^{-1/2}$  and  $1.4 \times 10^7 \text{m}^{-1/2}$ . Following Langitan and Lawn [26] approximation, the flaw size would be much closer to  $6 \mu\text{m}$  for this abrasion procedure and then  $3.7 \times 10^4 \text{m}^{-1/2} < R/c_f^{3/2} < 3.4 \times 10^5 \text{m}^{-1/2}$ . Auerbach's range applies just between both these approximations, so that theory agrees satisfactorily with experiments for small friction coefficient. However, Gilroy and Hirst [11] found that the upper limit of the Auerbach's range decreases as  $f$  increases, which is opposite to theoretical predictions.

## 6. Conclusion

Despite very limiting assumptions involved, the use of Hamilton equations for computing the stress field under a sliding hertzian contact and Mougnot and Maugis method for determining the crack equilibrium under such a contact can lead to analytical solutions which explain the main experimental results. The main conclusions of this study are following:

1. The strain energy release rate for partial cone crack was computed for various friction coefficients.
2. The initiation radii of the crack has been shown to reduce when  $f$  increases.
3. Auerbach's law is shown to apply even if  $f > 0$ , corresponding to the relatively flat maximum of the

TABLE II Critical load reductions ratio measured experimentally by Chiang and Evans [13] on various materials

T/N	$\lambda$ glass (pristine)	$\lambda$ glass (abraded)	$\lambda$ $\text{Si}_3\text{N}_4$
0.1	0.43	0.2	0.3
0.2	0.28	0.1	0.17

envelope of the  $\Phi$  curves plotting for various crack starting radii.

4. The computation of failure critical load can be performed by Equation 12 and provides a simple method for measuring fracture surface energy in the Auerbach's range

5. The reduction factor for the critical load computed with this method is in good agreement with the experimental values. The ratio between the maximum tensile stresses for sliding and normal cracks is also in good agreement with experiments.

6. Most aspects of the experimental results obtained by the previous authors can be explained by the analytical model.

## Acknowledgements

This study was supported by the "Direction des Recherches, Etudes et Techniques de la Délégation Générale pour l'Armement" of the French Department of Defense. The author wishes to express his thanks to Ph. Bensussan and D. Maugis for helpful discussions about this work.

## Appendix A

For using Hamilton's equations, two corrections are necessary: — for normal loading on the surface when  $r_0 < a$ ,  $\sigma_z$  and  $\tau_{xy}$  should be written in cartesian coordinates:

$$\sigma_z = \frac{3P}{2\pi a^3} [-(a^2 - r^2)^{1/2}] \quad (\text{A1})$$

$$\tau_{xy} = \frac{3P}{2\pi a^3} \left[ xy \frac{1-2\nu}{r^4} \{(a^2 - r^2)^{1/2} \times [-r^2 - \frac{2}{3}(a^2 - r^2)] + \frac{2}{3}a^3\} \right] \quad (\text{A2})$$

— the general expression of  $\sigma_x$  for tangential loading is:

$$\begin{aligned} \sigma_x = \frac{3Q}{2\pi a^3} \left\{ -x \left( \frac{\nu}{4} + 1 \right) \phi + \frac{axM}{r^4} \left[ \left( \frac{3}{2} - \frac{2x^2}{r^2} \right) \times (S\nu - 2Av + z^2) + \frac{x^2 z^2}{S} + \frac{7\nu r^2}{4} - 2\nu x^2 + r^2 \right] \right. \\ \left. + \frac{xzN}{r^4} \left\{ \left( \frac{3}{2} - \frac{2x^2}{r^2} \right) \left[ - \left( \frac{S}{6} + \frac{A}{3} \right) (1 - 2\nu) - \frac{1}{2}(z^2 + 3a^2) \right] + \frac{a^2 x^2}{S} - \frac{\nu r^2}{4} - \frac{7r^2}{4} \right\} \right. \\ \left. + \frac{4a^3 xz}{3r^4} \left( \frac{3}{2} - \frac{2x^2}{r^2} \right) (1 - 2\nu) \right\} \quad (\text{A3}) \end{aligned}$$

with  $Q = fP$ ;  $A = r^2 + z^2 - a^2$ ;  $S = (A^2 + 4a^2 z^2)^{1/2}$ ;  $r^2 = x^2 + y^2$ ;  $M = \left( \frac{S + A}{2} \right)^{1/2}$  and  $N = \left( \frac{S - A}{2} \right)^{1/2}$

## Appendix B

The equations of the stresses  $\sigma_r$  and  $\sigma_\theta$  proposed by Swain [10] from Mindlin [17] should be written:

$$\begin{aligned} \sigma_r = \frac{P}{\pi R^2} \left\{ \lambda \left[ \frac{1-2\nu}{4} \cos^{-2} \left( \frac{\phi}{2} \right) - \frac{3}{2} \cos \phi \sin^2 \phi \right] \right. \\ \left. + \mu \left[ \frac{1-2\nu}{2} \sin \phi (1 + \cos \phi)^{-2} - \frac{3}{2} \sin^3 \phi \right] \right\} \quad (\text{B1}) \end{aligned}$$

$$\begin{aligned} \sigma_\theta = \frac{P}{\pi R_2} \left( \lambda \left\{ \frac{1-2\nu}{2} \left[ \cos \phi - \frac{1}{2} \cos^{-2} \left( \frac{\phi}{2} \right) \right] \right\} \right. \\ \left. + \mu \left\{ \sin \phi [1 - (1 + \cos \phi)^{-2}] \right\} \right) \quad (\text{B2}) \end{aligned}$$

with  $\phi = tg^{-1}(x/z)$ ,  $\lambda$  and  $\mu$  being the magnitude of the vertical and horizontal components respectively. For a sliding contact  $\lambda = 0$  and  $\mu = f$ ,  $R^2 = x^2 + z^2$ .

## References

1. F. C. FRANK and B. R. LAWN, *Proc. R. Soc.* **A299** (1967) 291.
2. A. A. GRIFFITH, *Phil. Trans.* **A221** (1920) 163.
3. H. HERTZ, *J. Reine. Angew. Maths.* **92** (1881) 156.
4. M. T. HUBER, *Ann. Physik.* **14** (1904) 153.
5. T. R. WILSHAW, *J. Phys. D: Appl. Phys.* **4** (1971) 1567.
6. R. WARREN, *Acta Metall.* **26** (1978) 1759.
7. R. MOUGINOT and D. MAUGIS, *J. Mater. Sci.* **20** (1985) 4354.
8. F. AUERBACH, *Ann. Phys. Chem.* **43** (1891) 61.
9. B. R. LAWN, *Proc. R. Soc.* **A299** (1967) 307.
10. Y. ENOMOTO, *J. Mater. Sci.* **16** (1981) 3365.
11. D. R. GILROY and W. HIRST, *J. Phys. D: Appl. Phys.* **2** (1969) 1784.
12. B. HAMILTON and H. RAWSON, *ibid.* **B** (1970) L40.
13. B. R. LAWN, S. M. WIEDERHORN and D. E. ROBERTS, *J. Mater. Sci.* **19** (1984) 2561.
14. M. V. SWAIN, *Proc. R. Soc.* **A366** (1979) 575.
15. G. M. HAMILTON and L. E. GOODMAN, *J. Appl. Mech.* **33** (1966) 371.
16. G. M. HAMILTON, *Proc. Inst. Mech. Eng.* **197c** (1983) 53.
17. S. CHIANG and A. EVANS, *J. Amer. Ceram. Soc.* **66** (1) (1983)A 491.
18. B. D. POWELL and D. TABOR, *J. Phys. D: Appl. Phys.* **3** (1970) 783.
19. M. BARQUINS, D. MAUGIS and R. COURTEL, *C. R. Acad. Sc. Paris* **t276** (1973) A491.
20. S. WAY, *J. Appl. Mech.* **7** (1940) 147.
21. R. D. MINDLIN, *Physics* **7** (1936) 195.
22. R. MOUGINOT, Representations de l'état de contrainte sous contacts ponctuel et hertzien glissants. ETCA rapport interne (1986) to be published.
23. K. L. JOHNSON, J. J. O'CONNOR and A. C. WOODWARD, *Proc. R. Soc.* **A334** (1973) 95.
24. D. MAUGIS, *J. Mater. Sci.* **20** (1985) 3041.
25. O. O. ADEWOYE and T. F. PAGE, *Wear* **70** (1981) 37.
26. F. B. LANGITAN and B. R. LAWN, *J. Phys. D: Appl. Phys.* **40** (1969) 4009.
27. B. R. LAWN, *J. Appl. Phys.* **39** (1968) 4828.

Received 14 March  
and accepted 21 July 1986